

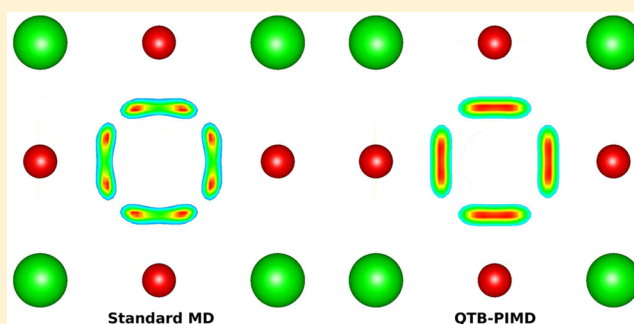
Quantum Thermal Bath for Path Integral Molecular Dynamics Simulation

Fabien Briec,[†] Hichem Dammak,^{*,†,‡} and Marc Hayoun[‡]

[†]Laboratoire Structures, Propriétés et Modélisation des Solides, CentraleSupélec, CNRS, Université Paris-Saclay, F-92295 Châtenay-Malabry, France

[‡]Laboratoire des Solides Irradiés, École Polytechnique, CNRS, CEA, Université Paris-Saclay, F-91128 Palaiseau, France

ABSTRACT: The quantum thermal bath (QTB) method has been recently developed to account for the quantum nature of the nuclei by using standard molecular dynamics (MD) simulation. QTB-MD is an efficient but approximate method when dealing with strongly anharmonic systems, while path integral molecular dynamics (PIMD) gives exact results but in a huge amount of computation time. The QTB and PIMD methods have been combined in order to improve the PIMD convergence or correct the failures of the QTB-MD technique. Therefore, a new power spectral density of the random force within the QTB has been developed. A modified centroid-virial estimator of the kinetic energy, especially adapted to QTB-PIMD, has also been proposed. The method is applied to selected systems: a one-dimensional double-well system, a ferroelectric phase transition, and the position distribution of an hydrogen atom in a fuel cell material. The advantage of the QTB-PIMD method is its ability to give exact results with a more reasonable computation time for strongly anharmonic systems.



1. INTRODUCTION

The quantum nature of nuclei can play a major role at low temperatures and/or in systems that contain light atoms. In this case, nuclear quantum effects cannot be neglected and must be taken into account in atomistic simulations. A standard way of including them is to use path integral methods,^{1–3} such as path integral molecular dynamics (PIMD), which provide exact quantum results, even for strongly anharmonic systems. Unfortunately, time correlation functions are not directly accessible and require the use of additional techniques such as ring polymer molecular dynamics⁴ or centroid molecular dynamics.⁵ Moreover, the computation time required for PIMD reduces its range of applicability, in particular when using a first-principles description of the interatomic forces.

Alternative techniques based on a modified Langevin equation have recently been proposed to include nuclear quantum effects in molecular dynamics (MD) simulations.^{6,7} Among them, the quantum thermal bath (QTB) method⁶ is an approximate approach that is very simple to implement in an existing MD code and yields accurate results for various types of systems.^{8–13} In addition, it requires the same amount of computation time as standard MD, and time correlation functions are directly accessible. The QTB method becomes approximate when dealing with strongly anharmonic systems and therefore suffers from the zero-point energy (ZPE) leakage.^{14,15} The ZPE leakage is a known problem^{16–19} in classical trajectories where energy flows from the high-frequency modes, with large zero-point energies, to low-frequency modes with smaller zero-point energies. An empirical

solution reducing the ZPE leakage within the QTB method has been attempted but with limited efficiency.^{14,15}

In this work, the QTB is combined with the PIMD method in order to (i) avoid the ZPE leakage within QTB-MD for strongly anharmonic systems and (ii) reduce the computation time of PIMD. The convergence of the PIMD is significantly accelerated, since fewer replicas are needed for convergence. The combination of QTB with PIMD is first described and then applied to selected systems: a one-dimensional double-well system, a ferroelectric phase transition, and the position distribution of an hydrogen atom in a fuel cell material.

2. COMBINING PATH INTEGRALS WITH THE QUANTUM THERMAL BATH (QTB)

The goal is to combine the PIMD with the QTB method in a way similar to that developed by Ceriotti et al.²⁰ In our case, the idea is to replace the classical thermostat applied to each bead of the polymer by the QTB. To achieve this, it is necessary to find the appropriate power spectral density of the random force, which will then be dependent on the number of replicas (P).

2.1. Equations of Dynamics. In both the PIMD and the combined QTB-PIMD formalisms, the equation of motion of each atom i ($i = 1, \dots, N$) of a replica s ($s = 1, \dots, P$) is given by

Received: December 4, 2015

Published: January 22, 2016

$$\dot{\mathbf{p}}_{i,s} = \left(\frac{1}{P}\right)\mathbf{f}_{i,s} - m_i\omega_p^2(2\mathbf{r}_{i,s} - \mathbf{r}_{i,s+1} - \mathbf{r}_{i,s-1}) - \gamma\mathbf{p}_{i,s} + \mathbf{R}_{i,s} \quad (1)$$

where $\mathbf{r}_{i,s}$, $\mathbf{p}_{i,s}$, and $\mathbf{f}_{i,s}$ are the atomic position, the momentum, and the force exerted by all the other atoms of the replica s . The spring constant between beads is equal to

$$m_i\omega_p^2 = \frac{m_i P k_B^2 T^2}{\hbar^2} \quad (2)$$

The last two terms of eq 1 correspond to the friction and stochastic forces of the thermostat, respectively.

The power spectral density of the random force (I_{R_i}) is obtained from the fluctuation–dissipation theorem:^{21,22}

$$I_{R_i}(\omega, T) = 2m_i\gamma\kappa(\omega, T) \quad (3)$$

In standard PIMD, when the Langevin thermostat is used, the stochastic force is a white noise and $\kappa(\omega, T) = k_B T$. For the combined QTB-PIMD, the power spectral density is ω -dependent and corresponds to the energy of the oscillator ω , which matches the energy $\theta(\omega, T)$ of the quantum harmonic oscillator when $P = 1$. $\kappa(\omega, T)$ will be determined in section 2.2. The correlation function of the random force satisfies the Wiener–Khinchin theorem:

$$\langle R_{i,s,\alpha}(t)R_{i,s,\alpha}(t + \tau) \rangle = \int_{-\infty}^{+\infty} I_{R_i}(\omega, T) \exp[-i\omega\tau] \frac{d\omega}{2\pi} \quad (4)$$

The random force $R_{i,s,\alpha}(t)$ is computed using the numerical technique described in the Appendix of ref 23.

2.2. Derivation of the Power Spectral Density.

Considering a one-dimensional (1D) harmonic potential energy: $V(x) = \frac{1}{2}m\omega^2 x^2$, the quantum mean square fluctuation of the position x at temperature T is given by

$$\langle x^2 \rangle = \left(\frac{1}{m\omega^2}\right)\theta(\omega, T) = \frac{\hbar}{2m\omega} \coth\left[\beta\left(\frac{\hbar\omega}{2}\right)\right] \quad (5)$$

where $\beta = 1/(k_B T)$. In the PIMD scheme, one can transform the coordinates of the P replicas, $x_1, \dots, x_s, \dots, x_p$, into normal modes, $q_0, \dots, q_k, \dots, q_{P-1}$ with pulsations

$$\omega_k^2 = \frac{\omega^2}{P} + 4\omega_p^2 \sin^2\left(\frac{k\pi}{P}\right) \quad (6)$$

and the mean square fluctuation is then obtained according to

$$\langle x^2 \rangle = \frac{1}{P} \sum_{k=0}^{P-1} \langle q_k^2 \rangle \quad (7)$$

The mean potential energy of the normal modes is equal to $\kappa(\omega_k, T)/2$ and then

$$\langle q_k^2 \rangle = \left(\frac{1}{m\omega_k^2}\right)\kappa(\omega_k, T) \quad (8)$$

Now, let us determine κ when performing QTB-PIMD. The function $\kappa(\omega, T)$ must allow one to recover the expected position fluctuation, which is given by eq 5:

$$\frac{1}{P} \sum_{k=0}^{P-1} \frac{1}{m\omega_k^2} \kappa(\omega_k, T) = \frac{\hbar}{2m\omega} \coth\left[\beta\left(\frac{\hbar\omega}{2}\right)\right] \quad (9)$$

Defining the dimensionless quantities

$$u = \beta\left(\frac{\hbar\omega}{2}\right) \quad (10)$$

$$h(u) = u \coth(u) \quad (11)$$

$$f_p^{(0)}(u) = \left(\frac{\beta}{P}\right)\kappa\left(\frac{2u}{\beta\hbar}\right) \quad (12)$$

eq 9 becomes

$$\sum_{k=0}^{P-1} \frac{u^2}{u_k} f_p^{(0)}(u_k) = h(u) \quad (13)$$

where u_k is the reduced pulsation, according to eqs 6 and 10:

$$u_k^2 = \frac{u^2}{P} + P \sin^2\left(\frac{k\pi}{P}\right) \quad (14)$$

In the definition of κ , using eq 9, all the normal modes are treated in the same way. There is an alternative definition²⁴ in which the normal mode at $k = 0$ (centroid of the ring polymer) is classically considered, i.e., $\kappa(\omega_0, T) = k_B T$. In this case, eq 9 becomes

$$\frac{1}{P}\left(\frac{k_B T}{m\omega_0^2}\right) + \frac{1}{P} \sum_{k=1}^{P-1} \frac{1}{m\omega_k^2} \kappa(\omega_k, T) = \frac{\hbar}{2m\omega} \coth\left[\beta\left(\frac{\hbar\omega}{2}\right)\right] \quad (15)$$

Using the same dimensionless quantities, eq 15 leads to a new equation to be solved:

$$\sum_{k=1}^{P-1} \frac{u^2}{u_k} f_p^{(1)}(u_k) = h(u) - 1 \quad (16)$$

Equations 13 and 16 can be solved by using the self-consistent iterative technique of Ceriotti et al.²⁰ The numerical calculation of $f_p^{(0)}$ ²⁵ and $f_p^{(1)}$ are reported in the Appendix.

2.3. Estimation of the Macroscopic Properties. In the PIMD method, the potential energy (U) is calculated using the expression

$$U = \frac{1}{P} \sum_s V(\mathbf{r}_{1,s}, \dots, \mathbf{r}_{N,s}) \quad (17)$$

whereas two expressions for the estimator of the kinetic energy are usually used; the primitive estimator, which is given by

$$K_{\text{prim}} = \sum_{i,s} \frac{\mathbf{p}_{i,s}^2}{2m_i} - \sum_{i,s} \frac{1}{2} m_i \omega_p^2 (\mathbf{r}_{i,s} - \mathbf{r}_{i,s+1})^2 \quad (18)$$

and the centroid-virial estimator, which is given by

$$K_{\text{Cvir}} = \left(\frac{3N}{2}\right)k_B T - \frac{1}{2P} \sum_{i,s} (\mathbf{r}_{i,s} - \mathbf{r}_i^c) \cdot \mathbf{f}_{i,s} \quad (19)$$

where $\mathbf{r}_i^c = \sum_s \mathbf{r}_{i,s}/P$ is the centroid of the ring polymer i . The last estimator is known to exhibit weaker fluctuations, which are insensitive to P , compared to the primitive estimator for which fluctuations grow with P .² Combining the QTB and PIMD methods includes a part of the quantum fluctuations in the momenta, i.e.,

$$\left\langle \sum_{i,s} \frac{\mathbf{p}_{i,s}^2}{2m_i} \right\rangle > \frac{3NPk_B T}{2} \quad (20)$$

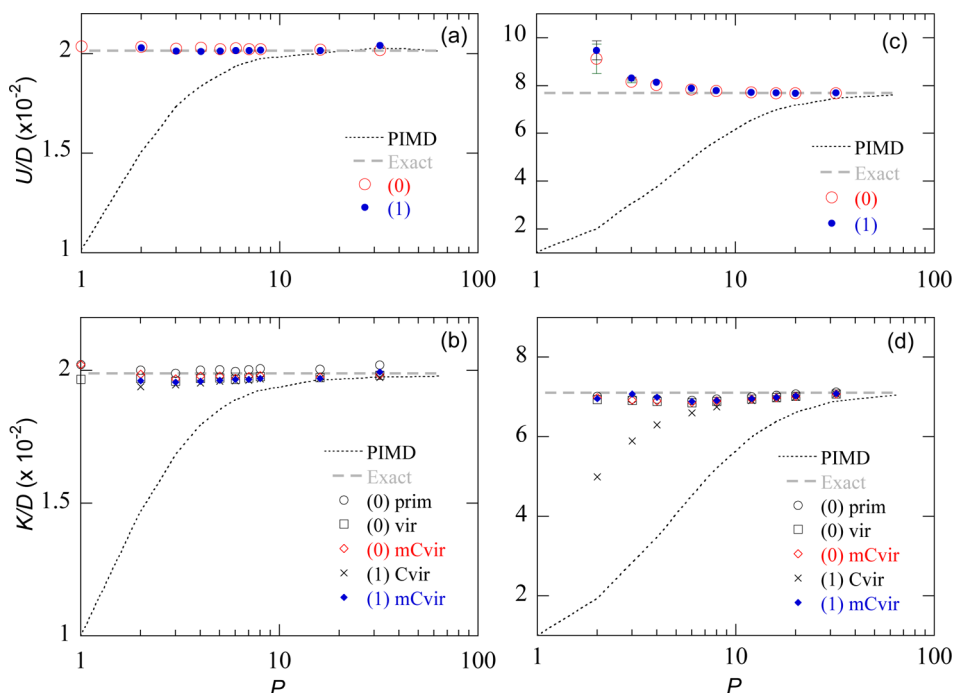


Figure 1. Convergence of the potential energy (U) and kinetic energy (K), as a function of the bead number for PIMD and QTBPIMD simulations using either $f_p^{(0)}$ or $f_p^{(1)}$, referenced hereafter as “(0)” and “(1)”, respectively. Morse potentials of (a, b) $\lambda^{-2} = 0.00145$ and (c, d) $\lambda^{-2} = 0.024$ are shown. The energies are normalized by the well depth D , and calculations were carried out at $T = 0.02D/k_B$. K values were obtained using either primitive (prim), virial (vir), centroid-virial (Cvir), or modified centroid-virial (mCvir) estimators, which are given by eqs 18, 23, 19, and 21, respectively. The exact values were derived by numerically solving the Schrödinger equation and occupying the resulting eigenstates with the proper Boltzmann factor.

Thus, eq 19 underestimates the kinetic energy for the QTBPIMD method and it is more suitable to replace the classical energy, $\frac{3}{2}Nk_B T$, by P multiplied by the kinetic energy of the N normal modes centroids, as follows:

$$K_{\text{mCvir}} = P \sum_i \frac{(\mathbf{p}_i^c)^2}{2m_i} - \frac{1}{2P} \sum_{i,s} (\mathbf{r}_{i,s} - \mathbf{r}_i^c) \cdot \mathbf{f}_{i,s} \quad (21)$$

where \mathbf{p}_i^c is the momentum of the centroid i . The factor P takes into account the factor $P^{1/2}$ between the centroid coordinate and the normal mode coordinate $\mathbf{q}_{i,0} = \sum_s \mathbf{r}_{i,s} / P^{1/2}$ of the ring i .

The two expressions described by eqs 19 and 21 are equivalent for any interatomic potential in the case of the original PIMD, but are equivalent only for harmonic potentials in the case of QTBPIMD using the $f_p^{(1)}$ function. In the case of an anharmonic potential, each centroid i , i.e., the normal mode $\mathbf{q}_{i,0}$, is coupled to the other normal modes of the corresponding polymer. Consequently, the centroid temperature is different from the thermostat temperature (QTBP), since some of the quantum effects are included in the momenta of the internal modes $\mathbf{q}_{i,k>0}$ of the polymer. On the other hand, only eq 21 may be used for the QTBPIMD, using the $f_p^{(0)}$ function, because, in this case, the dynamics of the centroid also includes quantum effects.

Next, we want to compare the two formulations of the QTBPIMD method using either the $f_p^{(0)}$ or $f_p^{(1)}$ functions (see eqs 13 and 16) and to choose the adequate kinetic energy estimator among eqs 18, 19, and 21. For this, let us consider a system for which the pressure is zero and, thus, the kinetic and potential contributions cancel each other out. This allows one to express the kinetic energy using the virial estimator (K_{vir}),^{26,27} from the general expression of the pressure:

$$pV = \frac{2}{3}K + \frac{1}{3P} \left\langle \sum_{i,s} \mathbf{r}_{i,s} \cdot \mathbf{f}_{i,s} \right\rangle \quad (22)$$

$$K_{\text{vir}} = -\frac{1}{2P} \sum_{i,s} \mathbf{r}_{i,s} \cdot \mathbf{f}_{i,s} \quad (23)$$

This estimator is used as a reference to validate the relevance of the other estimators. The test is performed on two cases of the Morse potential characterized by the dimensionless parameter λ , which is defined as

$$\frac{1}{\lambda^2} = \frac{\hbar^2 \alpha^2}{2mD} \quad (24)$$

where D is the depth of the well, α^{-1} the width of the well, and m the reduced mass. The anharmonicity of the potential can be expressed as the relative shift of the ground-state energy, with respect to the harmonic approximation value, $(4\lambda^2)^{-1}$. The first case is weakly anharmonic ($\lambda^{-2} = 0.0015$, as the case of the HCl molecule), whereas, for the second case, the anharmonicity is chosen to be more important ($\lambda^{-2} = 0.024$).

Figure 1 shows that the QTBPIMD method, either using $f_p^{(0)}$ or $f_p^{(1)}$, allows a faster convergence with the number of beads than the PIMD one, as expected. For both methods, the convergence is slower in the case of the more anharmonic potential. For the weakly anharmonic model, the potential energy (Figure 1a) remains almost constant, as a function of P , showing that the QTBP approach ($P = 1$) already provides a value very close to the exact one. The kinetic energy behaves similarly (Figure 1b) but is dependent on the estimator. For the two potential models, it is worth noting that K_{prim} and K_{Cvir} systematically give the highest and lowest values for the kinetic energy, respectively (Figures 1b and 1d). In contrast, K_{mCvir}

provides values very close to those obtained with K_{vir} , which is considered as a reference in this example. Figure 2 shows the

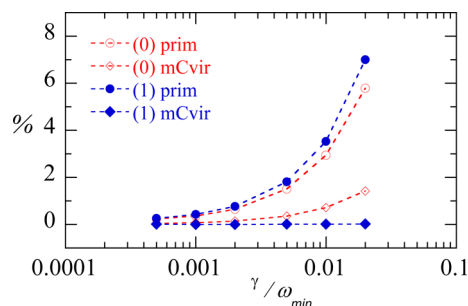


Figure 2. Effect of the effective friction coefficient (γ) on the kinetic energy obtained using the primitive (prim) and modified centroid-virial (mCvir) estimators. “(0)” and “(1)” correspond to QTB-PIMD simulations using $f_p^{(0)}$ and $f_p^{(1)}$ functions, respectively. The relative deviation from the virial estimator values, $(K - K_{\text{vir}})/K_{\text{vir}}$, is plotted. γ is normalized by the pulsation ω_{min} , which is equal to that of the centroid (normal mode $k = 0$ of the ring polymer) in the harmonic approximation: $\omega_{\text{min}} = \omega_0 = \omega/P^{1/2}$ (eq 6). The Morse potential is $\lambda^{-2} = 0.00145$, using $P = 4$ and $T = 0.02D/k_B$.

influence of the effective friction coefficient (γ) on the kinetic energy estimators. It is clearly shown that K_{mCvir} (eq 21) provides the better estimation and is particularly insensitive to γ when using the $f_p^{(1)}$ function, whereas the primitive estimator requires the use of a low value of γ , leading to an increase in the computation time.

This example shows that both definitions of the f_p functions (eqs 13 and 16) allow similar convergences of the potential and kinetic energies with the number of beads. The best estimator for the kinetic energy is the modified centroid-virial estimation that is given by eq 21. In the following sections, it is also shown that position distributions of atoms obtained by using $f_p^{(0)}$ or $f_p^{(1)}$ are very close.

3. APPLICATIONS

3.1. Position Distribution in a One-Dimensional Double-Well Potential. Let us consider a particle of mass m in a double-well potential:

$$V(x) = V_0 \left[\left(\frac{x}{a} \right)^2 - 1 \right]^2 \quad (25)$$

Using reduced units,

$$y = \frac{x}{a}, \quad \epsilon = \frac{E}{V_0} \quad (26)$$

for the position and the energy, respectively, the equation for the stationary wave functions ϕ is written as

$$-C \frac{d^2 \phi}{dy^2} + (y^2 - 1)^2 \phi = \epsilon \phi \quad (27)$$

where C is a parameter that is dependent on the barrier height (V_0) and the distance between the two wells ($2a$):

$$C = \frac{\hbar^2}{(2ma^2V_0)} \quad (28)$$

The numerical resolution of eq 27 shows that there exists a critical value for the parameter, $C_0 = 0.731778$, when the

ground-state energy is equal to V_0 . The eigenvalues rely on C , and we particularly observe that the energy of the ground state (ϵ_0) is lower than the height of the energy barrier (i.e., $\epsilon_0 < 1$) when $C < C_0$. The motivation behind using such a one-dimensional quartic double-well potential is to provide a simple model to check the ability of the QTB-PIMD method to recover the tunnel effect, in contrast to the original QTB approach.^{28,29} We investigate the position distribution of a particle in this double-well potential at a reduced temperature $T^* = k_B T/\epsilon_0 = 0.4$ for three values of the C parameter: 1, 0.3, and 0.1.

The position probability density, $\rho(y)$, which is obtained by QTB-PIMD simulation, is compared to the exact one, $\rho_0(y)$, which is obtained by numerically solving the Schrödinger equation and occupying the resulting eigenstates with the proper Boltzmann factor. The convergence of the density is evaluated by calculating the divergence factor (d_p),

$$d_p = \sqrt{\frac{\int_{-\infty}^{+\infty} (\rho - \rho_0)^2 dy}{\int_{-\infty}^{+\infty} \rho_0^2 dy}} \quad (29)$$

which is similar to the reliability factor used in the Rietveld method³⁰ to refine a theoretical line profile until it matches an experimental profile.

In all cases, the evolution of the divergence factor and the distributions as a function of P obtained with the QTB-PIMD method are similar when using either the $f_p^{(0)}$ function or the $f_p^{(1)}$ function.

Figure 3 shows the evolution of the divergence factor as a function of the number of beads for the three investigated cases. In the first case, the value of the C parameter ($C = 1$) is greater than the critical value C_0 (see eq 28). As shown by the divergence factor in Figure 3a, the distributions obtained with the QTB-PIMD and PIMD methods converge to the exact one, within an error of $d_p \approx 2\%$ at $P = 16$ and $P = 21$, respectively. Hence, the full convergence is especially difficult to reach in this case. Indeed, the exact distribution exhibits only one maximum, located at $y = 0$ (Figure 3d), while a poor convergence leads to a distribution with two maxima. One of these situations is illustrated by the QTB method, which fails dramatically, with an error of $d_p = 40\%$. In the other two cases, $C < C_0$ and all the position distributions show two maxima (see Figures 3e and 3f). For the QTB-PIMD simulation, the number of beads required to converge within an error of $d_p \approx 2\%$ decreases as C decreases; $P = 7$ for $C = 0.3$, and $P = 4$ for $C = 0.1$ (see Figures 3b and 3c). It is worth noting that, for the lowest value of C , the distribution obtained with the QTB method is in good agreement with the exact one. This case corresponds to high values of either the barrier height (V_0) or the distance between the two wells ($2a$), or the particle mass (m). In other words, the QTB method succeeds when the tunnel effect is not predominant.

In summary, the combination of the QTB and PIMD methods allows a better convergence with the number of beads. In fact, for a high accuracy in the position distribution, the gain obtained by QTB-PIMD, with respect to PIMD, is not as important and is lower than a factor of 2. In contrast, the advantage of the QTB-PIMD is more substantial—a gain of a factor of 3—with respect to the convergence of the total energy.

3.2. Ferroelectric–Paraelectric Phase Transition. We now investigate the BaTiO₃ (BTO) ferroelectric crystal, which

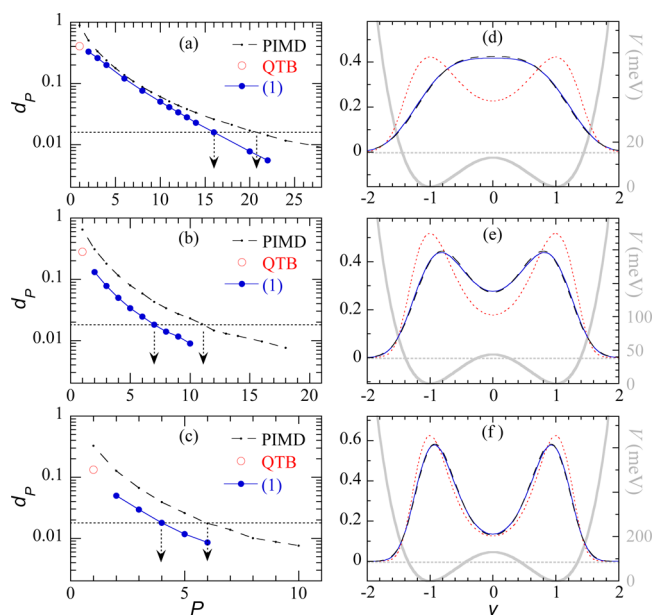


Figure 3. Divergence factor (d_p), as a function of the number of beads for the double-well potential (given by eq 27). Three cases of this potential are investigated: (a) $C = 1.0$, (b) $C = 0.3$, and (c) $C = 0.1$. Calculations have been carried out at a reduced temperature (T^*) of 0.4 for PIMD, QTBP, and QTBP-PIMD using the $f_p^{(1)}$ function. The arrows indicate the smallest numbers of beads obtained for $d_p < 2\%$. The calculated position distributions corresponding to the QTBP-PIMD case are shown (thin blue solid line) for (d) $P = 16$, (e) $P = 7$, and (f) $P = 4$, together with the exact solution (dashed line). The QTBP position distribution is also plotted (red dotted line) for comparison purposes. The potential energy curves are superimposed (heavy gray solid line), and the horizontal gray dotted lines represent the total energy of the system in each case; the V_0 values are deduced from C , using eq 28 for the hydrogen atom, and the distance between minima is fixed at $2a = 0.8 \text{ \AA}$.

is characterized by a complex multiple-well energy landscape affecting the polar degrees of freedom. In this compound, the quantum effects significantly decrease the phase transition temperatures by $\sim 30\text{--}50 \text{ K}$ ³¹ and strongly modify the shape of the pressure–temperature phase diagram,³² even at room temperature.

The ferroelectric properties of BTO are modeled by using the effective Hamiltonian of Zhong et al.,³³ which was derived from first-principles density-functional calculations. This approach yields an excellent description of its complex sequence of phase transitions: rhombohedral (R)—orthorhombic (O)—tetragonal (T)—cubic (C). The T–C phase-transition temperature (T_C) is equal to 300 K and 260 K, when using the standard MD and PIMD methods, respectively.³⁴

In this work, we investigate the convergence of the value of the phase-transition temperature (T_C), as a function of the number of beads, by performing either QTBP-PIMD or PIMD simulation in the isothermal–isobaric ensemble.

Figure 4 displays the polarization as a function of the temperature obtained by QTBP-PIMD, compared to the converged PIMD result. Favorably, the QTBP-PIMD method with 2 beads gives a transition temperature of $T_C = 257 \text{ K}$, which is very similar to that obtained by PIMD with $P = 16$ (259 K). In addition, the inset in Figure 4 shows that the convergence of the polarization of the ferroelectric phase is faster when using the $f_p^{(1)}$ function within the QTBP-PIMD method. In contrast, the use of the QTBP method (QTBP-PIMD

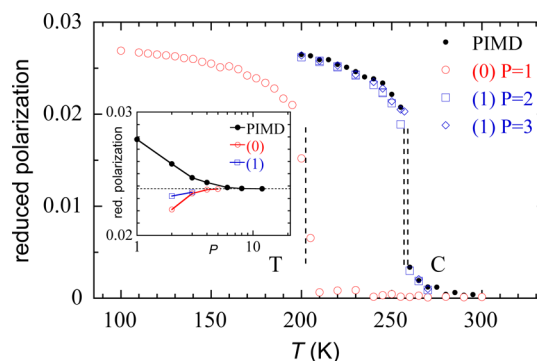


Figure 4. Temperature evolution of the reduced polarization associated with the tetragonal-to-cubic (T–C) ferroelectric transition, as obtained by PIMD ($P = 16$) and QTBP-PIMD simulations, using either $f_p^{(0)}$ or $f_p^{(1)}$, referenced as “(0)” and “(1)”, respectively. Vertical dashed lines show the quick convergence of the Curie temperature obtained by QTBP-PIMD: 202 K ($P = 1$), 257 K ($P = 2$), and 259 K ($P = 3$). The inset provides the convergence of the polarization at $T = 240 \text{ K}$ with the number of beads for the three methods.

with $P = 1$) strongly underestimates the value of T_C by $\sim 55 \text{ K}$. It is worth noting that the error of the QTBP method is fixed solely by two replicas when combining QTBP with PIMD. This means that the effects of the zero-point energy leakage associated with the use of the QTBP have been suppressed by the combination.

3.3. Proton Disorder in a Fuel-Cell Oxide: BaZrO₃. We now investigate the proton disorder in the cubic phase of BaZrO₃ (BZO).^{35,36} Indeed, it has been shown that (i) perovskite-type oxides (ABO₃) can exhibit high protonic conductivity³⁷ and (ii) quantum effects play an important role. Among these oxides, doped BZO exhibits one of the highest conductivities, combined with good chemical stability,^{37,38} which makes it a potential candidate as an electrolyte material for proton-conducting fuel cells.

The long-range migration of a proton in a BZO crystal is a combination of transfer and reorientation mechanisms. During the transfer step, the hydrogen atom jumps between the two neighboring O atoms while, during the reorientation stage, the H atom performs a rotation around the nearest O atom. There are two possible rotations: one around the Zr–O–Zr axis and one around an axis orthogonal to the Zr–O–Zr axis, with the H atom remaining in the same O–Zr–O plane.

The interactions between the atoms are modeled by an *ab initio*-based force field³⁹ that reproduces the *ab initio* computed activation energies for the transfer and reorientation mechanisms.^{39,40} The reactivity of the proton is included through the empirical valence bond model. No dopant is included in our simulations, so the distributions presented here illustrate the situation in a region far from the dopant atom. To ensure the electrical neutrality in the computations, a compensating uniform background charge is added. The MD simulations were performed within the canonical ensemble on a $3 \times 3 \times 3$ simulation box containing 136 atoms.

The three-dimensional (3D) position distribution of one proton in BZO is computed at $T = 300 \text{ K}$, using QTBP-PIMD and PIMD. As an illustration, the classical MD proton position distribution in the O–Zr–O plane is displayed in the top part of Figure 5. From this distribution, one can note that the H atom remains bonded to the same O atom, most of the time. One type of reorientation is essentially seen where the H atom performs a rotation around the nearest O atom and remains in

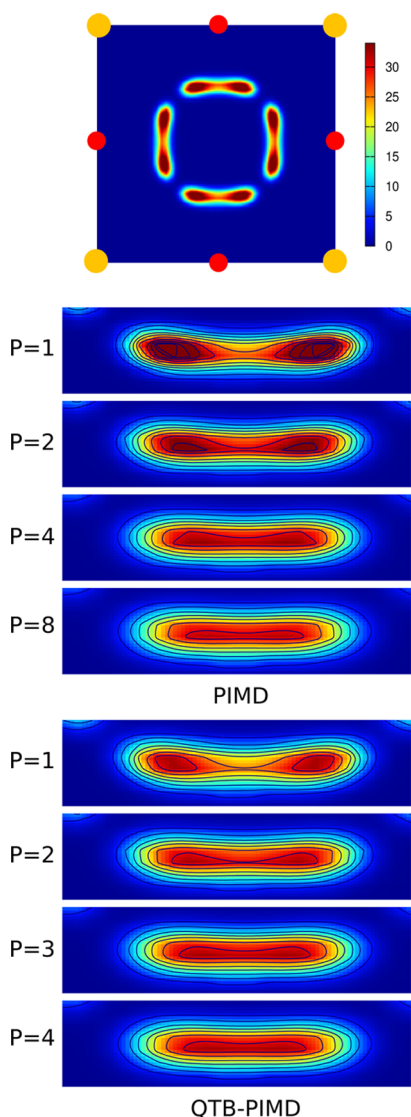


Figure 5. Position distribution of the proton in the O–Zr–O plane at $T = 300$ K, as obtained by PIMD and QTBPIMD simulations. The top image displays an example of the distribution in the unit cell (PIMD with $P = 1$), where one can distinguish the eight equivalent positions for the proton. The O and Zr atoms are shown by red and yellow full circles, respectively. The other images are enlargements of the distribution, including contour lines, to highlight the increase in the proton disorder by rotation around the neighboring O atom as the number of beads increases.

the same O–Zr–O plane. Figure 5 shows the evolution of the position distribution with the number of beads, as obtained by QTBPIMD and PIMD. Quantum effects are important at this temperature, since the classical distribution corresponding to PIMD with $P = 1$ is clearly different from the quantum distribution obtained by PIMD or QTBPIMD with high P values. In the classical case, the distribution exhibits two peaks, whereas in the quantum case, the proton freely rotates around the nearest O atom. In addition, the transfer mechanism is rarely observed at $T = 300$ K. For the QTBPIMD simulation, Figure 5 shows that the two peaks disappear for $P = 3$, and that the position distribution already converges to the exact one for $P = 4$. In contrast, the PIMD method requires a value of at least $P = 8$ for convergence. A more accurate comparison of the two methods is given in Figure 6, in which the corresponding

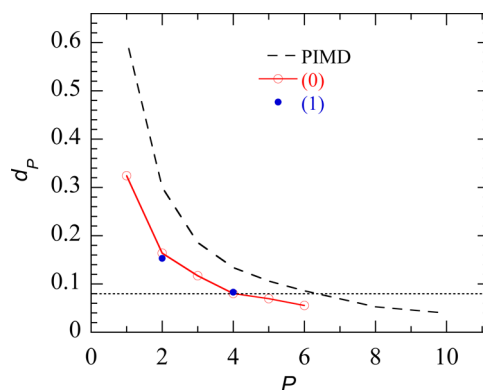


Figure 6. Divergence factor (d_p) (generalization of eq 29 in 3D), as a function of the number of beads for the proton distribution in BZO at $T = 300$ K obtained by PIMD and QTBPIMD simulations, using either $f_p^{(0)}$ or $f_p^{(1)}$, referenced hereafter as “(0)” and “(1)”, respectively. The horizontal dotted line allows one to determine the number of beads corresponding to $d_p = 0.08$.

divergence factors d_p (a generalization of eq 29 to 3D distributions) are plotted as a function of P . The PIMD calculations are converged within an error of $d_p = 8\%$ for $P = 6$, while the QTBPIMD method requires a smaller number of beads, $P = 4$. We conclude, as expected, that QTBPIMD is more efficient than the standard PIMD, since less replicas are needed for convergence.

4. CONCLUSION

We have combined the path integral MD (PIMD) method with the quantum thermal bath (QTB) approach. This combination can be seen in two ways. In the first way, the QTB is used as a thermostat applied to standard PIMD in order to improve the PIMD convergence. Compared to standard PIMD, this combination needs less replicas to converge—the gain is a factor of 2 or 3—since a part of the quantum effects is included directly in the dynamics of the beads through the QTB. In the second way, a small number of replicas of the path integral allows the correction of the failures of the QTB-MD. Indeed, the QTB-MD technique gives rather satisfactory macroscopic properties for weakly anharmonic systems, especially away from phase transitions and in the case of nonpredominant tunnel effects. Thus, QTB-MD remains an alternative method for those who are not interested in high-accuracy computations. Small failures of the QTB can be fixed by only two replicas in QTBPIMD. In contrast, when QTB-MD dramatically fails, QTBPIMD can address the problem at the price of high computational cost. The advantage of the QTBPIMD method is its ability to give exact results with a more reasonable computation time for strongly anharmonic systems, including the tunnel effect between two wells. Unfortunately, as in PIMD, the major drawback of the new method is that the time-dependent correlation functions are not directly accessible.

The combination with PIMD requires the modification of the power spectral density of the random force within the QTB. This spectral density is proportional to a reduced function (f_p), which can be defined in two ways. In one way, random forces are applied to each bead of the ring polymer ($f_p^{(0)}$). An alternative way is to apply random forces to the normal modes of the ring polymer ($f_p^{(1)}$), except for the centroid mode, which is addressed with a Langevin thermostat. It is shown that the $f_p^{(1)}$ function gives a better convergence of the macroscopic

quantities with the number of beads than $f_p^{(0)}$. Considering that some of the quantum fluctuations are included in the momenta through the QTB contribution, a modified centroid-virial estimator of the kinetic energy is proposed. This estimator is accurate and insensitive to the effective friction coefficient when using the $f_p^{(1)}$ function.

The combination procedure is similar to that presented by Ceriotti et al.²⁰ The iterative algorithm described in the Appendix to determine the f_p function is the same as that used to establish the g_p function of ref 20. The difference lies in the choice of the thermostat used to include the quantum effects. In the colored-noise thermostat (GLE) of Ceriotti et al.,⁷ the quantum effects are introduced through a dispersive friction coefficient, whereas, in the QTB case, the quantum effects are included through the power spectral density of the random force. The two methods are basically equivalent, but the QTB-MD method is easier to implement in a PIMD code. Knowing the f_p function, the random forces can be directly generated.²³ In contrast, the GLE method requires careful optimization of the different parameters in the equations of motion (see eq 8 in ref 20) in order to recover the quantum fluctuations.

The modified QTB is easy to include in any PIMD code, and the implementation does not increase its complexity. The combination of the QTB and the PIMD methods within first-principles descriptions is even more interesting. Such an implementation in the ABINIT code^{41,42} is in progress. Moreover, the possibility of combining the modified QTB with methods such as ring polymer molecular dynamics (RPMD)⁴ or centroid molecular dynamics (CMD)⁵ will allow one to go beyond PIMD. In this case, time-dependent correlation functions could be computed. Since the combination with the QTB consists of replacing the classical thermostat by the QTB, the combination with RPMD (thermostated RPMD has been recently proposed⁴³) or CMD would have the same complexity as that of the QTB-PIMD. Let us point out that the combination requires the use of physical bead masses instead of fictitious ones.

APPENDIX: SELF-CONSISTENT RESOLUTION OF EQUATIONS 13 AND 16

The $f_p^{(0)}$ and $f_p^{(1)}$ functions are determined through a self-consistent resolution of the equations.

In the case of the $f_p^{(0)}$ function, eq 13 can be reformulated by isolating the $k = 0$ term, for which

$$u_0 = \frac{u}{\sqrt{P}} \quad (\text{A1})$$

$$f_p\left(\frac{u}{\sqrt{P}}\right) = \frac{1}{P} \left[h(u) - \sum_{k=1}^{P-1} \frac{f_p(u_k)}{(u_k^2/u^2)} \right] \quad (\text{A2})$$

The "(0)" superscripts are omitted for the sake of simplicity. Before solving, eq A2 is rewritten using the function

$$F_p(u) = f_p\left(\frac{u}{\sqrt{P}}\right) \quad (\text{A3})$$

$$F_p(u) = \frac{1}{P} \left[h(u) - \sum_{k=1}^{P-1} \frac{F_p(u_k \sqrt{P})}{(u_k^2/u^2)} \right] \quad (\text{A4})$$

We choose an initial solution with good asymptotic behavior for eq A2:

$$F_p^{(0)}(u) = \frac{1}{P} h\left(\frac{u}{P}\right) \quad (\text{A5})$$

which matches the exact solution in the case for $P = 1$. Using this initial solution and following the work of Ceriotti et al.,²⁰ the equation is iteratively solved as

$$F_p^{(i+1)}(u) = \frac{\alpha}{P} \left[h(u) - \sum_{k=1}^{P-1} \frac{F_p^{(i)}(u_k \sqrt{P})}{(u_k^2/u^2)} \right] + (1 - \alpha) F_p^{(i)}(u) \quad (\text{A6})$$

where α is a weighting parameter whose value giving the best convergence is close to $1/P$. The random force of the QTB is generated from the power spectral density in the pulsation space in a range $[\omega_{\min}; \omega_{\max}]$. ω_{\max} and ω_{\min} are related to the MD time step δt and the time length of a MD trajectory, respectively. It results in the $F_p(u)$ function needing to be determined in the correlated range $[u_{\min}; u_{\max}]$. Unfortunately, eq A6 shows that F_p must be calculated for a value of $u_k P^{1/2}$, which reaches a value, $(u_{\max}^2 + P^2)^{1/2}$, that is greater than u_{\max} . To overcome this problem, the values of F_p for $u > u_{\max}$ are linearly extrapolated from the last 20% of the u range. The F_p function is obtained with enough accuracy over ~ 30 iterations in eq A6. Results show that the function $f_p(u)$, which is defined as $f_p(u) = F_p(u\sqrt{P})$ and is directly related to the spectral energy $\kappa(\omega, T)$, approaches $1/P$ for $u \rightarrow 0$ and $u/P^{3/2}$ for $u \rightarrow \infty$. Figure A1 presents the curves of the $f_p(u)$ solutions obtained for different values of P .

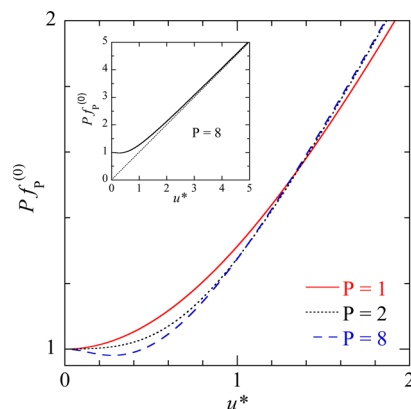


Figure A1. Plot of the $f_p^{(0)}$ function for different numbers of beads, P , as a function of $u^* = u/P^{3/2}$. The inset shows the asymptotic behavior at large values of u^* .

Now, let us consider the case of the $f_p^{(1)}$ function. Equation 16 can be reformulated by isolating the $k = 1$ term, for which

$$u_1^2 = \frac{u^2}{P} + P \sin^2\left(\frac{\pi}{P}\right) \quad (\text{A7})$$

$$\left(\frac{u^2}{u_1^2}\right) f_p(u_1) = \left[h(u) - 1 - \sum_{k=2}^{P-1} \frac{f_p(u_k)}{(u_k^2/u^2)} \right] \quad (\text{A8})$$

The "(1)" superscripts are omitted for the sake of simplicity. Before solving, eq A8 is rewritten using the function

$$F_p(u) = f_p(u_1) \quad (\text{A9})$$

$$F_p(u) = \frac{u^2}{u^2} \left[h(u) - 1 - \sum_{k=2}^{P-1} \left(\frac{u^2}{u_k^2} \right) F_p \left(\sqrt{Pu_k^2 - P^2 \sin^2 \left(\frac{\pi}{P} \right)} \right) \right] \quad (\text{A10})$$

We choose an initial solution with good asymptotic behavior for eq A8:

$$F_p^{(0)}(u) = \frac{1}{P-1} \left[h \left(\frac{u}{P} \right) - \frac{1}{P} \right] \quad (\text{A11})$$

Using this initial solution, the equation is iteratively solved as

$$F_p^{(i+1)}(u) = \alpha \left(\frac{u^2}{u^2} \right) \left[h(u) - 1 - \sum_{k=2}^{P-1} \left(\frac{u^2}{u_k^2} \right) F_p \left(\sqrt{Pu_k^2 - P^2 \sin^2 \left(\frac{\pi}{P} \right)} \right) \right] + (1-\alpha) F_p^{(i)}(u) \quad (\text{A12})$$

where α is a weighting parameter whose value giving the best convergence is close to $1/P$. The $F_p(u)$ function is determined following the above-mentioned procedure. Results show that the function

$$f_p(u) = F_p \left(\sqrt{Pu^2 - P^2 \sin^2 \left(\frac{\pi}{P} \right)} \right) \quad (\text{A13})$$

directly related to the spectral energy $\kappa(\omega, T)$, approaches $u/[(P-1)P^{1/2}]$ as $u \rightarrow \infty$. Figure A2 presents the curves of the $f_p(u)$ solutions obtained for different values of P .

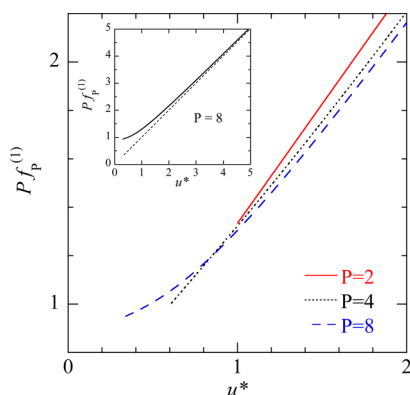


Figure A2. Plot of the $f_p^{(1)}$ function for different numbers of beads, P , as a function of $u^* = (P^{1/2}u - 1)/(P - 1)$. The inset shows the asymptotic behavior at large values of u^* .

Finally, the power spectral density thus obtained (eqs 3, 10, and 12) through the $f_p^{(0)}$ or $f_p^{(1)}$ functions,

$$I_{R_i} = 2m_i \gamma \left(\frac{P}{\beta} \right) f_p \left(\frac{\beta \hbar \omega}{2} \right) \quad (\text{A14})$$

corresponds to that of the random forces $R_{i,k,\alpha}$ to be applied to normal modes (i, k) of the ring polymer (i) . In the case of the $f_p^{(0)}$ function, one can show that the power spectral densities of the random forces applied to beads or to normal modes are equal. Hence, the random forces $R_{i,s,\alpha}$ can be directly generated according to eq 4. In contrast, for the $f_p^{(1)}$ function, since the centroid mode ($k = 0$) is not addressed in the same way as the other normal modes ($k > 0$), one must first generate the random forces $R_{i,k,\alpha}$ and then transform them to $R_{i,s,\alpha}$ by using the orthogonal transformation matrix C_{sk} :

$$R_{i,s,\alpha} = \sum_k C_{sk} R_{i,k,\alpha} \quad (\text{A15})$$

$$C_{sk} = \begin{cases} \sqrt{\frac{1}{P}} & \text{for } k = 0 \\ \sqrt{\frac{2}{P}} \cos\left(\frac{2\pi sk}{P}\right) & \text{for } 0 < k < \frac{P}{2} \\ \sqrt{\frac{1}{P}} (-1)^s & \text{for } k = \frac{P}{2} \\ \sqrt{\frac{2}{P}} \sin\left(\frac{2\pi sk}{P}\right) & \text{for } \frac{P}{2} < k < P \end{cases} \quad (\text{A16})$$

AUTHOR INFORMATION

Corresponding Author

*E-mail: hichem.dammak@centralesupelec.fr

Notes

The authors declare no competing financial interest.

ACKNOWLEDGMENTS

This work was performed using HPC resources from the "mesocentre" computing center of CentraleSupélec, which is supported by CentraleSupélec and CNRS.

REFERENCES

- Ceperley, D. M. *Rev. Mod. Phys.* **1995**, *67*, 279–355.
- Tuckerman, M. E. In *Statistical Mechanics: Theory and Molecular Simulation*; Ed.; Oxford University Press: New York, 2010, Chapter 12, pp 475–490.
- Marx, D.; Tuckerman, M. E.; Hutter, J.; Parrinello, M. *Nature* **1999**, *397*, 601–604.
- Craig, I. R.; Manolopoulos, D. E. *J. Chem. Phys.* **2004**, *121*, 3368–3373.
- Cao, J.; Voth, G. A. *J. Chem. Phys.* **1994**, *100*, 5106–5117.
- Dammak, H.; Chalopin, Y.; Laroche, M.; Hayoun, M.; Greffet, J. *J. Phys. Rev. Lett.* **2009**, *103*, 190601.
- Cerotti, M.; Bussi, G.; Parrinello, M. *Phys. Rev. Lett.* **2009**, *103*, 030603.
- Dammak, H.; Antoshchenkova, E.; Hayoun, M.; Finocchi, F. *J. Phys.: Condens. Matter* **2012**, *24*, 435402.
- Calvo, F.; Van-Oanh, N.; Parneix, P.; Falvo, C. *Phys. Chem. Chem. Phys.* **2012**, *14*, 10503–10506.
- Calvo, F.; Naumkin, F. Y.; Wales, D. J. *Chem. Phys. Lett.* **2012**, *551*, 38–41.
- Qi, T.; Reed, E. J. *J. Phys. Chem. A* **2012**, *116*, 10451–10459.
- Basire, M.; Borgis, D.; Vuilleumier, R. *Phys. Chem. Chem. Phys.* **2013**, *15*, 12591–12601.
- Bronstein, Y.; Depondt, P.; Finocchi, F.; Saitta, A. M. *Phys. Rev. B: Condens. Matter Mater. Phys.* **2014**, *84*, 214101.
- Bedoya-Martinez, O. N.; Barrat, J. L.; Rodney, D. *Phys. Rev. B: Condens. Matter Mater. Phys.* **2014**, *89*, 014303.
- Hernández-Rojas, J.; Calvo, F.; Noya, E. G. *J. Chem. Theory Comput.* **2015**, *11*, 861–870.
- Lu, D. H.; Hase, W. L. *J. Chem. Phys.* **1988**, *89*, 6723–6735.
- Miller, W. H.; Hase, W. L.; Darling, C. L. *J. Chem. Phys.* **1989**, *91*, 2863–2868.
- Bowman, J. M.; Gazdy, B.; Sun, Q. *J. Chem. Phys.* **1989**, *91*, 2859–2862.
- Habershon, S.; Manolopoulos, D. E. *J. Chem. Phys.* **2009**, *131*, 244518.
- Cerotti, M.; Manolopoulos, D. E.; Parrinello, M. *J. Chem. Phys.* **2011**, *134*, 084104.
- Callen, H. B.; Welton, T. A. *Phys. Rev.* **1951**, *83*, 34–40.

- (22) Kubo, R. *Rep. Prog. Phys.* **1966**, *29*, 255–284.
- (23) Chalopin, Y.; Dammak, H.; Laroche, M.; Hayoun, M.; Greffet, J. *J. Phys. Rev. B: Condens. Matter Mater. Phys.* **2011**, *84*, 224301.
- (24) Ceriotti, M.; Manolopoulos, D. E. *Phys. Rev. Lett.* **2012**, *109*, 100604.
- (25) The f_p function is different from the g_p function of Ceriotti et al.²⁰ because the authors used another formulation of the PIMD (at temperature $P \times T$). Indeed, $f_p(u) = (1/P)g_p(uP^{1/2})$.
- (26) Herman, M. F.; Bruskin, E. J.; Berne, B. J. *J. Chem. Phys.* **1982**, *76*, 5150–5155.
- (27) Parrinello, M.; Rahman, A. *J. Chem. Phys.* **1984**, *80*, 860–867.
- (28) Barrozo, A. H.; de Koning, M. *Phys. Rev. Lett.* **2011**, *107*, 198901.
- (29) Dammak, H.; Hayoun, M.; Chalopin, Y.; Greffet, J. *J. Phys. Rev. Lett.* **2011**, *107*, 198902.
- (30) Young, R. A., Ed. In *The Rietveld Method*; Oxford University Press: Oxford, U.K., 1993.
- (31) Zhong, W.; Vanderbilt, D. *Phys. Rev. B: Condens. Matter Mater. Phys.* **1996**, *53*, 5047–5050.
- (32) Iniguez, J.; Vanderbilt, D. *Phys. Rev. Lett.* **2002**, *89*, 115503.
- (33) Zhong, W.; Vanderbilt, D.; Rabe, K. *Phys. Rev. B: Condens. Matter Mater. Phys.* **1995**, *52*, 6301–6312.
- (34) Geneste, G.; Dammak, H.; Thiercelin, M.; Hayoun, M. *Phys. Rev. B: Condens. Matter Mater. Phys.* **2013**, *87*, 014113.
- (35) Azad, A. M.; Subramaniam, S. *Mater. Res. Bull.* **2002**, *37*, 85–97.
- (36) Akbarzadeh, A. R.; Kornev, I.; Malibert, C.; Bellaiche, L.; Kiat, J. *M. Phys. Rev. B: Condens. Matter Mater. Phys.* **2005**, *72*, 205104.
- (37) Kreuer, K. D. *Annu. Rev. Mater. Res.* **2003**, *33*, 333–359.
- (38) Colomban, P., Ed. In *Proton Conductors: Solids, Membranes and Gels—Materials and Devices*; Cambridge University Press: Cambridge, U.K., 1992; Part V.
- (39) Raiteri, P.; Gale, J. D.; Bussi, G. *J. Phys.: Condens. Matter* **2011**, *23*, 334213.
- (40) Ottochian, A.; Dezanneau, G.; Gilles, C.; Raiteri, P.; Knight, C.; Gale, J. D. *J. Mater. Chem. A* **2014**, *2*, 3127–3133.
- (41) Gonze, X.; et al. *Comput. Phys. Commun.* **2009**, *180*, 2582–2615.
- (42) Geneste, G.; Torrent, M.; Bottin, F.; Loubeyre, P. *Phys. Rev. Lett.* **2012**, *109*, 155303.
- (43) Rossi, M.; Ceriotti, M.; Manolopoulos, D. E. *J. Chem. Phys.* **2014**, *140*, 234116.